IEEE Access
Multidisciplinary ⋮ Rapid Review ⋮ Open Access Journal

Received 12 September 2023, accepted 7 October 2023, date of publication 12 October 2023, date of current version 18 October 2023.

Digital Object Identifier 10.1109/ACCESS.2023.3324038

APPLIED RESEARCH

Design and Experiments of Angular Motion Control for a Novel Unmanned Water-Powered Aerial Vehicle

CAO-TRI DINH[1,2], THINH HUYNH[2], DONG-HUN LEE[3], AND YOUNG-BOK KIM[1,3], (Senior Member, IEEE)

[1]Department of Intelligent Robot Engineering, Pukyong National University, Busan 48513, Republic of Korea
[2]Faculty of Vehicle and Energy Engineering, Ho Chi Minh City University of Technology and Education, Ho Chi Minh City 700000, Vietnam
[3]Department of Mechanical System Engineering, Division of Energy Transport System Engineering, Pukyong National University, Busan 48513, Republic of Korea

Corresponding author: Young-Bok Kim (kpjiwoo@pknu.ac.kr)

This work was supported in part by the National Research Foundation (NRF), South Korea, under Project BK21 FOUR (Smart Convergence and Application Education Research Center); and in part by the National Research Foundation of Korea (NRF) grant funded by the Korean Government (MSIT) under Grant 2022R1A2C1003486.

ABSTRACT Manned water-powered aerial vehicles have been widely applied in the entertainment field. By leveraging an abundant water source, these exhibit great potential for implementation in various fields, especially in high-risk environments such as rescue and firefighting operations. However, their maneuverability depends entirely on the riders' skills. Therefore, this paper proposes a novel unmanned water-powered aerial vehicle (UWAV) along with an angular motion controller for it. The proposed UWAV utilizes a nozzle rotation mechanism to adjust the water thrust's direction and replace the role of the rider in governing the system's motion. This study first derives a detailed mathematical model to describe its angular motion. Subsequently, a robust controller consists of two main components. The first part is a disturbance estimator formulated by an extended state observer (ESO), which estimates and compensates for disturbances in the control effort. The second part is an integral super-twisting sliding mode control (ISTSMC) law that incorporates the system's rotational dynamic characteristics and ensures the system's stability and robust tracking. Experiments are conducted to validate the proposed system through two scenarios: following step-like and sinusoidal references. The results demonstrated the feasibility of the design and the superiority of the proposed controller. Specifically, the control system achieves 56.98% lower root mean square error and requires 22.72% less control effort compared to that of the standalone ISTSMC.

INDEX TERMS Unmanned water-powered vehicle, nozzle rotation mechanism, integral super-twisting sliding mode control, extended state observer, angular motion control.

I. INTRODUCTION

The design of aerial water-powered vehicles (AWVs), such as jetpacks [1], [2], [3], [4], jet bikes [5], [6], and flyboards [7], [8], has found widespread application in the entertainment field. Essentially, an AWV comprises three main components: a water pump, a flexible water hose, and a board assembly. In this setup, water flows from the water pump to the board assembly through the water hose. On the board assembly, water is jetted out at the water outlet port, generating thrust force that lifts both the board assembly and rider. Manipulating the AWV requires two individuals. The first person operates the watercraft, housing the water pump underneath. The second person, known as the flyboard rider, controls the flyboard's motion by adjusting the center of gravity and water flow throttle. The flyboard rider demonstrates complex skills to perform intricate movements. In addition to entertainment applications, water-jet propulsion devices, taking advantage of abundant water sources, are also used in fire accidents to put out flames [9] in special spaces where

The associate editor coordinating the review of this manuscript and approving it for publication was Min Wang.

traditional firefighting methods struggle to reach. However, one can see that the maneuverability of the AWVs depends heavily on the rider's complex techniques. Furthermore, the total mass of the board assembly, including the operator, is quite substantial, limiting the flexibility of the board assembly. These factors bring significant barriers for AWVs when applied in other fields such as intricate space exploration, rescue, and fire extinguishing.

To overcome these limitations, unmanned water-powered aerial vehicles (UAWVs) have been developed for high-level specialized applications. Their fundamental structure is still similar to traditional AWVs. However, the board assembly involves an automatic drive mechanism to replace the role of the human operator. Several studies have investigated drive mechanism solutions, primarily classified into three types: weight-shifting, flow-regulating, and nozzle rotation mechanisms.

The weight-shifting mechanism represents an intuitive approach to driving the head assembly by mimicking the actions of the human operator on a flyboard. Dinh et al. [10] proposed two sets of mass moving horizontally on the head to govern its horizontal motions. However, the results show the system exhibits a non-minimum phase phenomenon, uncontrollable yaw movement, and an increase in the overall mass of the head system. Thus, despite its simple design, these characteristics introduce challenges for practical implementation.

Regulating the water flow is another solution for the UWAV's drive mechanism. This uses two or more valves to distribute the water flow differently from a manifold to multiple nozzles, thereby generating varying thrust between them. Liu and Zhou [11] investigated this type with two sets of orthogonal flow-regulated mechanisms. However, the design results in uncontrollable yaw movement. Lee et al. [12] addressed this issue by independently distributing water to four nozzles. Nonetheless, this system, in practical implementation, requires more actuators than necessary. Huynh and Kim [13] proposed a new arrangement with three valves to regulate the water flow among four thrust nozzles. Even so, this mechanism generally requires powerful and high-precision actuators to operate the valves under high water pressure. Moreover, other drawbacks are also realized, such as the flow fluctuation due to the valves' opening and the limited range of operation caused by the nozzles' fixed posture.

The third approach utilizes multiple rotating nozzles to adjust the water force acting on the head, known as the nozzle rotation mechanism. Liu and Zhou [11] also proposed a nozzle-gimbaled UWAV using four servos to drive two nozzles through a soft tube. Although experimental results with a small-scale prototype demonstrated the ability of 6-DoF motion, the system non-minimum phase phenomenon was captured, introducing a challenge for control system design. Furthermore, the two-nozzle type exhibits lower system stability compared to the four-nozzle variant. To overcome these drawbacks, another research group from Tohoku University, Japan has investigated the Dragon Firefighter (DFF) system [14], [15], [16], [17], [18], the one equipped with two fixed and two biaxial nozzles. However, this arrangement can only provide a very limited maneuverability of the head assembly. Additionally, the water pipe is stiff, short, and positioned on the side. Thus, the flexibility of the entire system is predicted to be poor. In [19], Thinh et al. proposed another nozzle rotation mechanism and conducted performance comparisons with the previous weight-shifting and flow-regulating ones. This design includes three servos to rotate four nozzles, in which the two nozzles are linked together. Simulation results indicate that the proposed nozzle rotation mechanism outperforms the others, showing superior tracking performance of the head assembly and oscillation reduction for the water hose. Moreover, compared to previous approaches in [11], [14], [15], [16], [17], and [18], the design in [19] can overcome significant drawbacks, especially in the non-minimum phase phenomenon [11] and poor maneuverability [14], [15], [16], [17], [18]. However, it still retains certain disadvantages, and its feasibility is still not verified in practical experiments. In summary, the comparison of the structural design of related studies can be summarized in Table 1.

In terms of control strategies, both linear and nonlinear approaches have been applied to UWAVs. In particular, the well-known derivative (D) [14], [15], [16], [17] and proportional-derivative (PD) [11], [18] controllers, which rely solely on output feedback, have been implemented for the purpose of stabilizing the system. Except [18], none of them can prove the system stability analytically. Moreover, these controllers are very simple, and the experiment results indicate that they could not stabilize the system effectively. To enhance the system stability and provide tracking capability, a servo controller [10], [19] has been proposed with full state feedback and an integral action. However, the influence of disturbances, hose dynamics, and nonlinear characteristics on the system stability remains significant. To deal with these factors, a cascade sliding mode controller (SMC) [12] and a robust composite [13] controller have been applied. In particular, the SMC [12] provides robust tracking of the head assembly in the presence of disturbances. However, the main drawback is its discontinuous control law which causes a chattering phenomenon and puts a challenge to actuators. Additionally, in [13], the distinct characteristics of the system such as coupling, under actuation, and the water hose's dynamics were considered for control system design. However, the other external disturbances, such as drag, wind, the effect of the ground, ceiling, etc. were ignored in the design process and their influence on the entire system has not been validated. Overall, one can conclude that the nonlinear controllers demonstrate robustness and tracking capabilities compared to the above-mentioned linear counterpart. Nevertheless, both [12], [13] are still in the simulation stage, and their effectiveness in practical experiments has not yet been verified. In order to highlight the advantages and disadvantages of the previous related

TABLE 1. Comparison in terms of structural designs of related studies.

Drive mechanism	Description	Advantage	Disadvantage	Ref.
Weight-shifting mechanism	The weights slide on the head to distribute the loads on it, mimicking the actions of the human operator.	- The design is simple and intuitive.	- The non-minimum phase phenomenon is captured. - The yaw movement is uncontrollable.	[10],[19]
Water flow-regulating mechanism	The valves distribute the water flow differently from a manifold to multiple nozzles, thereby generating varying thrust between them.	- The design is simple. - The built-in valves and minimal moving parts provide high durability.	- The actuators are required powerful and high-precision to operate the valves under high water pressure. - The operational range is limited due to the fixed posture of the nozzles. - The yaw movement is limited in [11].	[11-13], [19]
Nozzle rotation mechanism	The nozzles are driven by the servos to provide multi-directional water thrust.	- The 6-DoF motion of the head assembly is controllable.	- The non-minimum phase phenomenon is captured.	[11]
		- The water hose fluctuation is reduced.	- The flexibility of the entire system is limited.	[14-18]
		- The 6-DoF motion of the head assembly is controllable. - The water hose fluctuation is reduced. - The operating range of the head assembly can be extended.	- The design is complex. - The arrangement of actuators still provides low flexibility in the head assembly.	[19]

TABLE 2. Comparison in terms of control strategies of related studies.

Type	Controller	Advantage	Disadvantage	Ref.
Linear	D	- Only output feedback is required. - The design is simple.	- It only deals with the stabilization problem. - The UWAV cannot be stabilized effectively. - The stability has not been proven analytically (except [18]).	[14-17]
	PD			[11][18]
	Servo	- The tracking capability is provided. - The design is simple.	- The influences of disturbances are still significant. - The controller's effectiveness has not been verified experimentally.	[10][19]
Nonlinear	Sliding mode	- The robust tracking is achieved under the presence of disturbances.	- The chattering phenomenon is captured. - The controller's effectiveness has not been verified experimentally.	[12]
	Robust composite	- The completed model with the water hose is considered in the control system design. - The control function is continuous. - The robust tracking for the head and stabilization of the hose are both achieved.	- The effect of external disturbances has not yet been considered. - The controller's effectiveness has not been verified experimentally.	[13]

studies, a comparison of the control strategies is made in Table 2.

Motivated to tackle these abovementioned issues, we propose a novel UWAV utilizing the nozzle rotation mechanism and then design a robust angular motion controller. The proposed vehicle draws inspiration from the one described in [19], thus inheriting the abovementioned advantages compared to the others. However, our proposed design has several distinctive features as follows: (1) every nozzle module is independently driven by a servo. This configuration provides a large-angle attitude controllability. Besides, it allows the 6-DoF motion of the head assembly to be guaranteed even in the case of a constant water flow rate; (2) the swivel ball joint, which makes the whole system complex and unnecessarily heavy, is eliminated. Although this tradeoff may amplify the water hose influence on the head assembly, it is able to be addressed in control system design. The proposed controller consists of two components: (1) an extended state observer (ESO) for disturbance estimation and compensation (e.g., drag, wind, water hose effects, ground, ceiling, etc.); and (2) an integral super-twisting sliding mode control (ISTSMC) law with considerations for rotational dynamics to ensure system stability and robust tracking. Compared to the abovementioned studies, the advantages of the proposed controller can be outlined as follows: (1) the rotational dynamic characteristics are modelled and compensated directly; (2) a continuous control law provides alleviation to the chattering phenomenon; (3) an integral action is considered in the sliding manifold to eliminate the steady-state error; and (4) the disturbances can be estimated and compensated. As in result, the proposed controller is expected to achieve good tracking performance and robustness against disturbances. In summary, the main contributions of this study can be outlined as follows:

- A novel design of the UWAV using a nozzle rotation mechanism is proposed.
- A mathematical model describing the angular motion of the head assembly is derived.
- A robust nonlinear controller is developed for the angular motion of the head assembly. It comprises the ESO

and the ISTSMC to ensure the tracking performance and robustness against disturbances.
- Experiments are conducted under the step-like and sinusoidal references, validating the proposed system.

The rest of the paper is organized as follows. Section II describes the system and its mathematical model. Section III presents the design of the angular motion controller. Section IV showcases the experimental results and discussions. Finally, Section V outlines conclusions.

II. PROPOSED SYSTEM MODEL

A. SYSTEM DESCRIPTION

Our proposed UWAV is introduced in Fig. 1. The system operates as follows: the water pump supplies water to the inlet port of the robot head through a flexible water hose. The robot head features four steering nozzles, evenly spaced 90 [deg] apart. Each steering nozzle is connected to the water distributor via a swivel joint. The cross-sectional area of the nozzle's outlet port is significantly smaller than that of the water inlet port, facilitating accelerated water flow to generate thrust force. Furthermore, the nozzles are positioned at a 75 [deg] angle relative to the horizontal plane, enhancing stability.

Each nozzle is directly actuated by a servo, which is connected through a servo arm and a linkage, ensuring a 1:1 synchronization between the servo's rotation angle and the angle of the rotary nozzle mechanism. This configuration enables the nozzle's rotation range to span ±45 [deg]. By manipulating the control water force direction and the water flow rate, the proposed UWAV can move freely in three-dimensional space. Additionally, a circuit box is placed on the top of the head, which houses various electric components including sensors, microcontrollers, etc.

B. HEAD ASSEMBLY MODELLING

The body-fixed frame (BFF) $\boldsymbol{OXYZ}$ and the Earth-fixed frame (EFF) $\boldsymbol{O_bX_bY_bZ_b}$ are used to describe the movement of the head assembly. Specifically, in the EFF, the $\boldsymbol{X}$-axis, $\boldsymbol{Y}$-axis, and $\boldsymbol{Z}$-axis point along the North, East, and upward directions, respectively. Additionally, the BFF is positioned on the head assembly, where its $\boldsymbol{X}_b$-axis, $\boldsymbol{Y}_b$-axis, and $\boldsymbol{Z}_b$-axis align with the longitudinal, lateral, and vertical axes, respectively. The coordinate system and dimension notation of the robot head are shown in Fig 2. The kinematic relationship of two coordinates is represented by:

$$\dot{\boldsymbol{\varphi}} = \boldsymbol{T}_b^E \boldsymbol{\omega}_b \tag{1}$$

where $\dot{\boldsymbol{\varphi}} = [\dot{\phi} \ \dot{\theta} \ \dot{\psi}]^T$ is the Euler angle rate in EFF, and $\boldsymbol{\omega}_b = [\omega_{xb} \ \omega_{yb} \ \omega_{zb}]^T$ is the angular velocity in BFF. Additionally, $\boldsymbol{T}_b^E$ is the transformation matrix between the angular velocity and the Euler angle rate [20].

To simplify the formulation of the mathematical model for the head assembly, let us make the following crucial assumptions: (A1) the mass of the nozzle module is small and can be neglected, (A2) the main water distributor, along

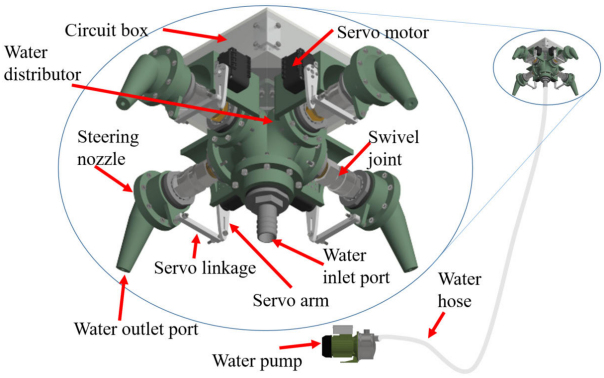

FIGURE 1. The proposed unmanned water-powered aerial system.

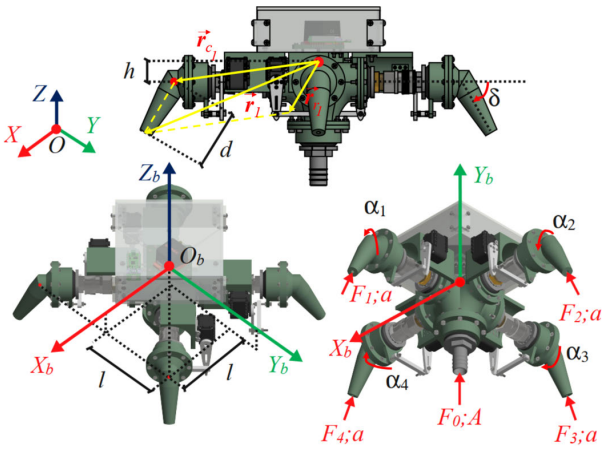

FIGURE 2. The coordinate system and dimension of the head assembly.

with its contained water volume, is non-deformable. (A3) The water flow is frictionless [21].

The head assembly, isolated from the water hose, is mathematically described using Euler equation:

$$\boldsymbol{J}\dot{\boldsymbol{\omega}}_b + \boldsymbol{\omega}_b \times \boldsymbol{J}\boldsymbol{\omega}_b = \boldsymbol{\tau}_b \tag{2}$$

where $\boldsymbol{J} = diag(J_{bx}, J_{by}, J_{bz})$ represents the inertia matrix of the head assembly, which is assumed to be diagonal. The symbol "$\times$" represents the cross product.

On the right-hand side of (2), the torques $\boldsymbol{\tau}_b$ acting on the head are provided as follows:

$$\boldsymbol{\tau}_b = \boldsymbol{\tau}_t + \boldsymbol{\tau}_d \tag{3}$$

in which, $\boldsymbol{\tau}_t$ and $\boldsymbol{\tau}_d$ represent the torques respectively generated by water thrust and other external disturbances such as the wind gust, ceiling, ground effect, and particularly the water hose effect.

From the differential linear momentum equation for incompressible flow and with the third assumption, the generated torque is obtained as follows:

$$\boldsymbol{\tau}_t = -\sum_{i=1}^{4} \dot{m}_i \boldsymbol{r}_i \times \boldsymbol{V}_i - \sum_{i=1}^{4} \dot{m}_i \boldsymbol{r}_i \times (\boldsymbol{\omega}_b \times \boldsymbol{r}_i) \tag{4}$$

In (4), $i = 1, 2, 3, 4$ denotes the i^{th} nozzle, and $\dot{m}_i$ represents the mass flow rate of water at the outlet port. Moreover,

$\boldsymbol{r}_i$ signifies the position of the nozzle's outlet, and $\boldsymbol{V}_i$ denotes the velocity of the water flow at this port.

The order position of each nozzle, numbered from 1 to 4, is detailed in Fig. 2. One can see that the position of the i^{th} nozzle, $\boldsymbol{r}_i$, is a composite vector of $\boldsymbol{r}_{\boldsymbol{c}_i}$ and $\boldsymbol{r}_{r_i}$. Specifically, in the BFF, $\boldsymbol{r}_{\boldsymbol{c}_i}$ is the position of the center of rotation of the i^{th} nozzle, while $\boldsymbol{r}_{r_i}$ varies following the rotation α_i of that nozzle. In particular, $\boldsymbol{r}_{r_i}$, with a length of d, is initialized at the BFF's origin and along the $\boldsymbol{Y}_b$-axis. Subsequently, $\boldsymbol{r}_{r_i}$ follows a sequence of rotations δ, α_i and $-45 + 90\,(i-1)$ [deg] about the $\boldsymbol{X}_b$-, $\boldsymbol{Y}_b$-, and $\boldsymbol{Z}_b$-axes, respectively. Additionally, the velocity vector $\boldsymbol{V}_i$ of the water flow at the nozzle outlet is determined in a similar manner. In short, they are given by the following equations:

$$\begin{aligned}
\boldsymbol{r}_i &= \boldsymbol{r}_{\boldsymbol{c}_i} + \boldsymbol{R}^{Z_b}_{-45+90(i-1)}\boldsymbol{R}^{Y_b}_{\alpha_i}\boldsymbol{R}^{X_b}_{-\delta}\,[0 \;\; d \;\; 0]^T\,,\\
\boldsymbol{V}_i &= \dot{\boldsymbol{r}}_i + \boldsymbol{R}^{Z_b}_{-45+90(i-1)}\boldsymbol{R}^{Y_b}_{\alpha_i}\boldsymbol{R}^{X_b}_{-\delta}\left[0 \;\; \frac{\dot{m}_i}{\rho a} \;\; 0\right]^T,\\
\boldsymbol{r}_{\boldsymbol{c}_1} &= [l \;\; l \;\; -h]^T\,, \quad \boldsymbol{r}_{\boldsymbol{c}_2} = [-l \;\; l \;\; -h]^T\,,\\
\boldsymbol{r}_{\boldsymbol{c}_3} &= [-l \;\; -l \;\; -h]^T\,,\\
\boldsymbol{r}_{\boldsymbol{c}_4} &= [l \;\; -l \;\; -h]^T
\end{aligned} \tag{5}$$

The term $\boldsymbol{R}^{(\cdot_1)}_{(\cdot_2)}$ represents the rotation matrix with $(\cdot_1)$ denoting the rotation axis of the BFF and $(\cdot_2)$ denoting the rotation angle. The term ρ and a represent water density and the cross-sectional area of the nozzle outlet, respectively.

Finally, by substituting (3), (4), and (5) into (2) and applying the kinematic relationship from (1), the rotational motion of the head assembly is obtained in the EFF as follows:

$$\begin{aligned}
\ddot{\boldsymbol{\varphi}} &= \boldsymbol{T}\dot{\boldsymbol{\varphi}} + \boldsymbol{T}^E_b\boldsymbol{u} + \boldsymbol{d},\\
\boldsymbol{T} &= -\boldsymbol{T}^E_b\left(\dot{\boldsymbol{T}}^E_b\right)^{-1} + \boldsymbol{T}^E_b\boldsymbol{\xi}\left(\boldsymbol{T}^E_b\right)^{-1},\\
\boldsymbol{\xi} &= diag\,\{\xi_1, \xi_2, \xi_3\}\,, \quad \boldsymbol{d} = \begin{bmatrix} d_\phi & d_\theta & d_\psi \end{bmatrix}^T
\end{aligned} \tag{6}$$

where:

$$\begin{aligned}
\xi_1 &= -\frac{1}{J_{bx}}\left(h^2 + l^2 + \frac{\sqrt{2}}{2}dl\cos\delta + \frac{d^2\cos^2\delta}{2}\right)\dot{m}_0,\\
\xi_2 &= -\frac{1}{J_{by}}\left(h^2 + l^2 + \frac{\sqrt{2}}{2}dl\cos\delta + \frac{d^2\cos^2\delta}{2}\right)\dot{m}_0,\\
\xi_3 &= -\frac{1}{J_{bz}}\left(2l^2 + \sqrt{2}dl\cos\delta + d^2\cos^2\delta\right)\dot{m}_0
\end{aligned} \tag{7}$$

Here, $\boldsymbol{u}$ represents the control effort, and it is interpreted as follows:

$$\begin{aligned}
\boldsymbol{u} &= \boldsymbol{M}\,[\sin\alpha_1 \;\; \sin\alpha_2 \;\; \sin\alpha_3 \;\; \sin\alpha_4]^T\,,\\
\boldsymbol{u} &= \begin{bmatrix} u_\phi & u_\theta & u_\psi \end{bmatrix}^T\,, \quad \boldsymbol{M} = \begin{bmatrix} a_1 & -a_1 & -a_1 & a_1\\ a_2 & a_2 & -a_2 & -a_2\\ a_3 & a_3 & a_3 & a_3 \end{bmatrix},\\
a_1 &= \frac{1}{J_{bx}}\frac{\sqrt{2}\,h\dot{m}_0^2\sin\delta}{32\rho a}, \quad a_2 = \frac{1}{J_{by}}\frac{\sqrt{2}\,h\dot{m}_0^2\sin\delta}{32\rho a},\\
a_3 &= \frac{1}{J_{bz}}\frac{\sqrt{2}\,l\dot{m}_0^2\sin\delta}{16\rho a}
\end{aligned} \tag{8}$$

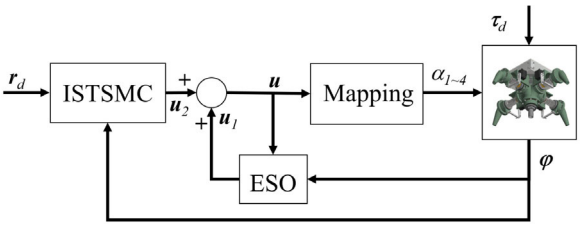

FIGURE 3. The proposed control scheme.

Furthermore, vector $\boldsymbol{d}$ represents the remaining terms after substitution, including the higher-order terms, the input-output coupling terms, and the external disturbances.

III. ANGULAR MOTION CONTROL SYSTEM DESIGN

The objective of the controller is to control the roll, pitch, and yaw angles such that the angular motion of the robot head can follow a desired reference with a tracking error as small as possible even in the presence of disturbances. In the first stage of development, the water flow rate is kept at a fixed value to investigate the nozzle rotation mechanism. Therefore, the angular motion of the robot head entirely depends on the water thrust direction. The proposed nonlinear control framework is shown in Fig. 3, where the control law $\boldsymbol{u}$ consists of two parts $\boldsymbol{u}_1$ and $\boldsymbol{u}_2$.

In particular, the first part $\boldsymbol{u}_1$ is constructed based on the ESO to estimate and compensate for disturbances in the control effort. The second part $\boldsymbol{u}_2$ is formed from the ISTSMC scheme incorporating the rotational dynamic characteristics of the head assembly, allowing the head assembly to robustly follow the desired trajectory. The proposed controller can be expressed as follows:

$$\boldsymbol{u} = \boldsymbol{u}_1 + \boldsymbol{u}_2 \tag{9}$$

A. DISTURBANCE ESTIMATION

Assuming the disturbances $\boldsymbol{d}$ are differential and bounded by a non-negative constant γ_O such that $\|\dot{\boldsymbol{d}}\| \le \gamma_O$, the plant model (6) treats the disturbances as the extended state. This can be expressed as in the following state-space form with $\boldsymbol{x}_1 = \boldsymbol{\varphi}$:

$$\begin{cases}
\dot{\boldsymbol{x}}_1 = \boldsymbol{x}_2\\
\dot{\boldsymbol{x}}_2 = \boldsymbol{T}\boldsymbol{x}_2 + \boldsymbol{T}^E_b\boldsymbol{u} + \boldsymbol{x}_3\\
\dot{\boldsymbol{x}}_3 = \dot{\boldsymbol{d}}
\end{cases} \tag{10}$$

The nonlinear ESO is designed as follows:

$$\begin{cases}
\boldsymbol{e}_O = \boldsymbol{x}_1 - \hat{\boldsymbol{x}}_1\\
\dot{\hat{\boldsymbol{x}}}_1 = \hat{\boldsymbol{x}}_2 + \boldsymbol{L}_1\boldsymbol{e}_O\\
\dot{\hat{\boldsymbol{x}}}_2 = \boldsymbol{T}\boldsymbol{x}_2 + \boldsymbol{T}^E_b\boldsymbol{u} + \hat{\boldsymbol{x}}_3 + \boldsymbol{L}_2\boldsymbol{e}_O\\
\dot{\hat{\boldsymbol{x}}}_3 = \boldsymbol{L}_3\boldsymbol{e}_O
\end{cases} \tag{11}$$

In the above formula, $\hat{\boldsymbol{x}}_j$ $(j = 1, 2, 3)$ represents the observer state variable, $\boldsymbol{L}_j = diag\left\{l_{j\phi}, l_{j\theta}, l_{j\psi}\right\} > 0$ represents the observer gain to be chosen. Defining $\tilde{\boldsymbol{x}}_j = \boldsymbol{x}_j - \hat{\boldsymbol{x}}_j$

as the estimation error, the observer error dynamics can be written as:

$$\dot{\tilde{\boldsymbol{x}}} = \bar{\boldsymbol{A}}\tilde{\boldsymbol{x}} + \bar{\boldsymbol{B}}\dot{\boldsymbol{x}}_3 \tag{12}$$

where:

$$\tilde{\boldsymbol{x}} = \begin{bmatrix} \tilde{\boldsymbol{x}}_1 \\ \tilde{\boldsymbol{x}}_2 \\ \tilde{\boldsymbol{x}}_3 \end{bmatrix} \quad \bar{\boldsymbol{A}} = \begin{bmatrix} -\boldsymbol{L}_1 & \boldsymbol{I}_3 & \boldsymbol{O}_3 \\ -\boldsymbol{L}_2 & \boldsymbol{O}_3 & \boldsymbol{I}_3 \\ -\boldsymbol{L}_3 & \boldsymbol{O}_3 & \boldsymbol{O}_3 \end{bmatrix}, \ \bar{\boldsymbol{B}} = \begin{bmatrix} \boldsymbol{O}_3 \\ \boldsymbol{O}_3 \\ \boldsymbol{I}_3 \end{bmatrix} \tag{13}$$

For the convergence of the estimation errors, Gao [22] suggested that all poles of the characteristic polynomial of the observer should be placed at its bandwidths. Equivalently, one can have:

$$\boldsymbol{L}_1 = 3\boldsymbol{\omega}_0, \quad \boldsymbol{L}_2 = 3\boldsymbol{\omega}_0^2, \ \boldsymbol{L}_3 = \boldsymbol{\omega}_0^3 \tag{14}$$

where $\boldsymbol{\omega}_0 = diag\left\{\omega_\phi, \omega_\theta, \omega_\psi\right\}$ presents the observer bandwidths for the roll, pitch, and yaw angles.

Lemma [22], [23]: The observer error dynamics (12) are said to be uniformly ultimately bounded (UUB) with the chosen gains.

The Proof of Lemma: Let us define a Lyapunov function candidate: $V_1 = \tilde{\boldsymbol{x}}^T\bar{\boldsymbol{P}}\tilde{\boldsymbol{x}}$, where $\bar{\boldsymbol{P}} \in R^{9\times 9}$ is symmetric and positive definite. Since $\bar{\boldsymbol{A}}$ is Hurwitz thanks to Gao's suggestion, then there exists $\bar{\boldsymbol{P}}$ satisfies the Lyapunov equation $\bar{\boldsymbol{A}}^T\bar{\boldsymbol{P}} + \bar{\boldsymbol{P}}\bar{\boldsymbol{A}} = -\boldsymbol{I}$. The time derivative of V_1 is derived as follows:

$$\begin{aligned} \dot{V}_1 &= \dot{\tilde{\boldsymbol{x}}}^T\bar{\boldsymbol{P}}\tilde{\boldsymbol{x}} + \tilde{\boldsymbol{x}}^T\bar{\boldsymbol{P}}\dot{\tilde{\boldsymbol{x}}} \\ &= \tilde{\boldsymbol{x}}^T\left(\bar{\boldsymbol{A}}^T\bar{\boldsymbol{P}} + \bar{\boldsymbol{P}}\bar{\boldsymbol{A}}\right)\tilde{\boldsymbol{x}} + \dot{\boldsymbol{x}}_3^T\boldsymbol{B}^T\bar{\boldsymbol{P}}\tilde{\boldsymbol{x}} + \tilde{\boldsymbol{x}}^T\bar{\boldsymbol{P}}\boldsymbol{B}\dot{\boldsymbol{x}}_3 \\ &\le -\|\tilde{\boldsymbol{x}}\|\left(\|\tilde{\boldsymbol{x}}\| - 2\gamma_0\lambda_{\max}\left(\bar{\boldsymbol{P}}\right)\right) \end{aligned} \tag{15}$$

where $\lambda_{\max}(.)$ is the maximum eigenvalues of the corresponding matrix. From (15), $\dot{V}_1 \le 0$ whenever the state $\tilde{\boldsymbol{x}}$ satisfies the condition $\|\tilde{\boldsymbol{x}}\| \ge 2\gamma_0\lambda_{\max}\left(\bar{\boldsymbol{P}}\right)$. Hence, the ESO is stable and the state vector $\tilde{\boldsymbol{x}}$ converges. One can conclude that the uniform ultimate boundedness (UUB) of the ESO is achieved with the ultimate bound $\sqrt{\frac{4\gamma_0^2\lambda_{\max}^3(\bar{\boldsymbol{P}})}{\lambda_{\min}(\bar{\boldsymbol{P}})}}$ [23]. □

Then, to compensate for the disturbances, the first part of the control law is designed as follows:

$$\boldsymbol{u}_1 = -\left(\boldsymbol{T}_b^E\right)^{-1}\hat{\boldsymbol{x}}_3 \tag{16}$$

B. INTEGRAL SUPER-TWISTING SLIDING MODE CONTROL

Given a desired reference $\boldsymbol{r}_d = \begin{bmatrix}\phi_d & \theta_d & \psi_d\end{bmatrix}^T$ in the EFF, the tracking error between the desired reference and the plant output is denoted as $\boldsymbol{e} = \begin{bmatrix}e_\phi & e_\theta & e_\psi\end{bmatrix}^T = \boldsymbol{r}_d - \boldsymbol{\varphi}$. Assuming that the desired reference is bounded and twice continuously differentiable, consider the following sliding manifold:

$$\boldsymbol{s} = \begin{bmatrix}s_\phi & s_\theta & s_\psi\end{bmatrix}^T = \dot{\boldsymbol{e}} + \boldsymbol{n}_1\boldsymbol{e} + \boldsymbol{n}_2\int_0^t \boldsymbol{e}(\tau)d\tau \tag{17}$$

where $\boldsymbol{n}_1 = diag\left\{n_{1\phi}, n_{1\theta}, n_{1\psi}\right\}$ and $\boldsymbol{n}_2 = diag\left\{n_{2\phi}, n_{2\theta}, n_{2\psi}\right\}$ represent 3-by-3 diagonal gain matrices, both of them are positive definite. The time derivative of $\boldsymbol{s}$ is derived as:

$$\dot{\boldsymbol{s}} = \ddot{\boldsymbol{e}} + \boldsymbol{n}_1\dot{\boldsymbol{e}} + \boldsymbol{n}_2\boldsymbol{e} = \ddot{\boldsymbol{r}}_d - \boldsymbol{T}\dot{\boldsymbol{\varphi}} - \boldsymbol{T}_b^E\boldsymbol{u} - \boldsymbol{x}_3 + \boldsymbol{n}_1\dot{\boldsymbol{e}} + \boldsymbol{n}_2\boldsymbol{e} \tag{18}$$

The control law $\boldsymbol{u}_2$ is designed as follows:

$$\boldsymbol{u}_2 = \left(\boldsymbol{T}_b^E\right)^{-1} \cdot \left(\begin{array}{l} \ddot{\boldsymbol{r}}_d - \boldsymbol{T}\dot{\boldsymbol{\varphi}} + \boldsymbol{n}_1\dot{\boldsymbol{e}} + \boldsymbol{n}_2\boldsymbol{e} \\ \\ +\boldsymbol{n}_3\begin{bmatrix} |s_\phi|^{\frac{1}{2}}\, sign(s_\phi) \\ |s_\theta|^{\frac{1}{2}}\, sign(s_\theta) \\ |s_\psi|^{\frac{1}{2}}\, sign(s_\psi) \end{bmatrix} + \boldsymbol{n}_4\begin{bmatrix} \int_0^t sign\left(s_\phi(\tau)\right)d\tau \\ \int_0^t sign\left(s_\theta(\tau)\right)d\tau \\ \int_0^t sign\left(s_\psi(\tau)\right)d\tau \end{bmatrix} \end{array} \right) \tag{19}$$

where $\boldsymbol{n}_3 = diag\left\{n_{3\phi}, n_{3\theta}, n_{3\psi}\right\}$ and $\boldsymbol{n}_4 = diag\left\{n_{4\phi}, n_{4\theta}, n_{4\psi}\right\}$ represent the diagonal gain matrices, both of which are positive definite. The notation *sign* denotes the signum function.

Substitute the proposed control law (9), (16) and (19) into (18), the dynamics of the sliding manifold is interpreted as follows:

$$\begin{cases} \dot{s}_h = -n_{3h}\,|s_h|^{\frac{1}{2}}\, sign\,(s_h) + v_h \\ \dot{v}_h = -n_{4h} sign\,(s_h) - \dot{\tilde{x}}_{3h} \end{cases} \quad h = \phi, \theta, \psi \tag{20}$$

The right-hand side of (20) is discontinuous, its solution is understood in the sense of Filippov [24]. Additionally, let us define $\boldsymbol{\zeta}_h = [\zeta_{1h} \ \ \zeta_{2h}]^T = \begin{bmatrix}|s_h|^{\frac{1}{2}}\, sign\,(s_h) & v_h\end{bmatrix}^T$. Then, the time derivative of $\boldsymbol{\zeta}_h$ is given by:

$$\begin{aligned} \dot{\boldsymbol{\zeta}}_h &= |s_h|^{\frac{-1}{2}}\boldsymbol{A}_h\boldsymbol{\zeta}_h + \boldsymbol{B}_h\dot{\tilde{x}}_{3h}, \\ \boldsymbol{A}_h &= \begin{bmatrix} -\frac{1}{2}n_{3h} & -\frac{1}{2} \\ n_{4h} & 0 \end{bmatrix}, \quad \boldsymbol{B}_h = \begin{bmatrix} 0 \\ 1 \end{bmatrix} \end{aligned} \tag{21}$$

Theorem: For the UWAV whose dynamics are presented in (6), the control law (9), (16) and (19) can guarantee the stability of the entire system if and only if there exists a symmetric positive definite matrix $\boldsymbol{P}_h \in R^{2\times 2}$ and a positive scalar γ_h such that the following inequality (22) holds.

$$\begin{bmatrix} \boldsymbol{A}_h^T\boldsymbol{P}_h + \boldsymbol{P}_h\boldsymbol{A}_h + \boldsymbol{C}_h^T\boldsymbol{C}_h & \boldsymbol{P}_h\boldsymbol{B}_h \\ \boldsymbol{B}_h^T\boldsymbol{P}_h & -\gamma_h^2 \end{bmatrix} \le 0 \tag{22}$$

where $\boldsymbol{C}_h = \begin{bmatrix}1 & 0\end{bmatrix}$.

The Proof of Theorem: To preserve the system stability with the proposed control law, we considered the following Lyapunov function candidate:

$$V_2 = \sum_{h=\phi,\theta,\psi} \boldsymbol{\zeta}_h^T\boldsymbol{P}_h\boldsymbol{\zeta}_h \tag{23}$$

Despite V_2 being discontinuous on the set $s_h = 0$, its time derivative exists almost everywhere since the trajectories of (20) cross $s_h = 0$ when $v_h \neq 0$ every time before reaching the origin [25]. One can see $\dot{\tilde{x}}_{3h}$ is bounded thanks to the stability of the ESO, which is demonstrated in the ***lemma***. Additionally, consider the following inequality:

$$\dot{V}_2 + \sum_{h=\phi,\theta,\psi} |s_h|^{\frac{1}{2}} \left(1 - \gamma_h^2 \dot{\tilde{x}}_{3h}^2\right) \leq 0, \quad \gamma_h > 0 \tag{24}$$

and note that $|\zeta_{1h}| = |s_h|^{\frac{1}{2}}$. The inequality (24) is interpreted as follows:

$$\begin{aligned}
&\dot{V}_2 + \sum_{h=\phi,\theta,\psi} |s_h|^{\frac{1}{2}} \left(1 - \gamma_h^2 \dot{\tilde{x}}_{3h}^2\right) \\
&= \sum_{h=\phi,\theta,\psi} \left(\left(\dot{\boldsymbol{\zeta}}_h^T \boldsymbol{P}_h \boldsymbol{\zeta}_h + \boldsymbol{\zeta}_h^T \boldsymbol{P}_h \dot{\boldsymbol{\zeta}}_h\right) + |s_h|^{\frac{1}{2}} \left(1 - \gamma_h^2 \dot{\tilde{x}}_{3h}^2\right)\right) \\
&= \sum_{h=\phi,\theta,\psi} |s_h|^{\frac{-1}{2}} \left(\boldsymbol{\zeta}_h^T \left(\boldsymbol{A}_h^T \boldsymbol{P}_h + \boldsymbol{P}_h \boldsymbol{A}_h\right) \boldsymbol{\zeta}_h \right. \\
&\quad + |s_h|^{\frac{1}{2}} \dot{\tilde{x}}_{3h}^T \boldsymbol{B}_h^T \boldsymbol{P}_h \boldsymbol{\zeta}_h + |s_h|^{\frac{1}{2}} \boldsymbol{\zeta}_h^T \boldsymbol{P}_h \boldsymbol{B}_h \dot{\tilde{x}}_{3h} \\
&\quad \left. + \boldsymbol{\zeta}_h^T \boldsymbol{C}_h^T \boldsymbol{C}_h \boldsymbol{\zeta}_h - \gamma_h^2 |s_h|^{\frac{1}{2}} |s_h|^{\frac{1}{2}} \dot{\tilde{x}}_{3h}^2\right) \\
&= \sum_{h=\phi,\theta,\psi} |s_h|^{\frac{-1}{2}} \begin{bmatrix} \boldsymbol{\zeta}_h \\ |s_h|^{\frac{1}{2}} \dot{\tilde{x}}_{3h} \end{bmatrix}^T \\
&\quad \times \begin{bmatrix} \boldsymbol{A}_h^T \boldsymbol{P}_h + \boldsymbol{P}_h \boldsymbol{A}_h + \boldsymbol{C}_h^T \boldsymbol{C}_h & \boldsymbol{P}_h \boldsymbol{B}_h \\ \boldsymbol{B}_h^T \boldsymbol{P}_h & -\gamma_h^2 \end{bmatrix} \begin{bmatrix} \boldsymbol{\zeta}_h \\ |s_h|^{\frac{1}{2}} \dot{\tilde{x}}_{3h} \end{bmatrix}
\end{aligned} \tag{25}$$

Then, from the expression in (25), one can see inequality (24) is satisfied for all values of $\begin{bmatrix} \boldsymbol{\zeta}_h \\ |s_h|^{\frac{1}{2}} \dot{\tilde{x}}_{3h} \end{bmatrix}$ if and only if the matrix $\begin{bmatrix} \boldsymbol{A}_h^T \boldsymbol{P}_h + \boldsymbol{P}_h \boldsymbol{A}_h + \boldsymbol{C}_h^T \boldsymbol{C}_h & \boldsymbol{P}_h \boldsymbol{B}_h \\ \boldsymbol{B}_h^T \boldsymbol{P}_h & -\gamma_h^2 \end{bmatrix}$ is negative semi-definite. The value of this matrix is dependent on the variables $\boldsymbol{A}_h$, $\boldsymbol{P}_h$ and γ_h. It is worth noting that $\boldsymbol{A}_h$ contains the controller's gains n_{3h} and n_{4h}. Thus, if these gains are chosen such that there exist $\boldsymbol{P}_h$ and γ_h making (22) hold, the stability of the system is guaranteed and good performance can be achieved. □

Remark 1: The inequality (24) is equivalent to the boundedness on the $\boldsymbol{L}_2$ gain of each orientation being γ_h, in which the $\boldsymbol{L}_2$ gain is denoted by: $\boldsymbol{L}_2 := \sup_{\left\|\dot{\tilde{x}}_{3h}\right\|_2 \neq 0} \left(\left\|\boldsymbol{\zeta}_h\right\|_2 / \left\|\dot{\tilde{x}}_{3h}\right\|_2\right)$. There are many solutions to this bilinear matrix inequality (BMI) in (22), one of which is equivalent to the solution of the smallest upper bound minimization problem [26]:

$$\begin{aligned}
&\underset{\boldsymbol{A}_h, \boldsymbol{P}_h}{\text{minimize}} \ \gamma_h \\
&\text{s.t} \ \boldsymbol{P}_h > 0, \quad \begin{bmatrix} \boldsymbol{A}_h^T \boldsymbol{P}_h + \boldsymbol{P}_h \boldsymbol{A}_h + \boldsymbol{C}_h^T \boldsymbol{C}_h & \boldsymbol{P}_h \boldsymbol{B}_h \\ \boldsymbol{B}_h^T \boldsymbol{P}_h & -\gamma_h^2 \end{bmatrix} \leq 0
\end{aligned} \tag{26}$$

The smallest upper bound on the $\boldsymbol{L}_2$ gain can be achieved via (26) by minimizing γ_h over $\boldsymbol{A}_h$, $\boldsymbol{P}_h$, and γ_h such that $\boldsymbol{P}_h > 0$ and $\boldsymbol{A}_h^T \boldsymbol{P}_h + \boldsymbol{P}_h \boldsymbol{A}_h + \boldsymbol{C}_h^T \boldsymbol{C}_h + \gamma_h^2 \boldsymbol{P}_h \boldsymbol{B}_h \boldsymbol{B}_h^T \boldsymbol{P}_h \leq 0$.

Remark 2: The integral action in (17) helps to eliminate steady-state errors [27], [28]. The traditional integral action, however, can lead to large overshoots and long settling times [29]. In the spirit of [30] and [31], to overcome these drawbacks, let us replace the traditional integral action by $\boldsymbol{\sigma}$, which can be interpreted as follows:

$$\begin{aligned}
\boldsymbol{s} &= \dot{\boldsymbol{e}} + \boldsymbol{n}_1 \boldsymbol{e} + \boldsymbol{n}_2 \boldsymbol{\sigma} \\
\dot{\boldsymbol{\sigma}} &= \boldsymbol{n}_1^{-1} \left(-\boldsymbol{n}_2 \boldsymbol{\sigma} + \kappa \, sat\left(\frac{\boldsymbol{s} - \dot{\boldsymbol{e}}}{\kappa}\right)\right)
\end{aligned} \tag{27}$$

in which, *sat* denotes the saturation function, with $\kappa > 0$ the boundary layer thickness, and is designed as follows:

$$\begin{aligned}
&sat\left(\frac{s_h - \dot{e}_h}{\kappa}\right) \\
&= \begin{cases} 1 & s_h - \dot{e}_h > \kappa \\ -1 & s_h - \dot{e}_h < -\kappa \\ \dfrac{s_h - \dot{e}_h}{\kappa} & -\kappa \leq s_h - \dot{e}_h \leq \kappa \end{cases} \qquad h = \phi, \theta, \psi
\end{aligned} \tag{28}$$

By substituting (28) into (27), one can see that inside the boundary $-\kappa \leq s_h - \dot{e}_h \leq \kappa$ of the function, $\dot{\sigma}_h = e_h$. Outside of the boundary, $|\dot{\sigma}_h| < e_h$. Therefore, this modified integral action ensures that large overshoots can be avoided.

Remark 3: The super-twisting algorithm is introduced to reduce, but not completely eliminate, the chattering phenomenon [32]. For further chattering attenuation, the *sign*(.) function can be replaced by *sat*(.) function in practical applications. However, using the latter only ensures the convergence of the sliding manifold to a boundary layer instead of restricting it onto the switching surface [33].

IV. EXPERIMENTAL STUDIES

A. EXPERIMENT SETUP

The experiments were conducted to validate both the proposed controller and the design of the head assembly. In Fig. 4, the head assembly is suspended from the frame using the swivel-ball joint, allowing for free rotation. The head assembly is positioned 1.4 [m] above the ground. Detailed specifications of the system are provided in Table 3. Additionally, it is worth noting that the moment of inertia of the head was obtained from Autodesk Inventor Professional 2021 software.

The tuned gain matrices of the proposed controller are shown in Table 4. One can notice that the tracking and disturbances observer performances of the head assembly depend on the values of the ISTSMC's gains and the ESO's gains, respectively. Specifically, increasing the values of gains $\boldsymbol{n}_3$ and $\boldsymbol{n}_4$ enhances the tracking performance [25]. However, excessively large values of $\boldsymbol{n}_3$ and $\boldsymbol{n}_4$ can lead to the chattering phenomenon. Moreover, increasing the bandwidths $\boldsymbol{\omega}_0$ of ESO improves the disturbances estimation performance, but it may also amplify the measurement noises from the sensor.

The proposed control law is implemented on a 32-bit OpenRB-150 microcontroller, with a Cortex-M0 core. The system utilizes this microcontroller to read data from the

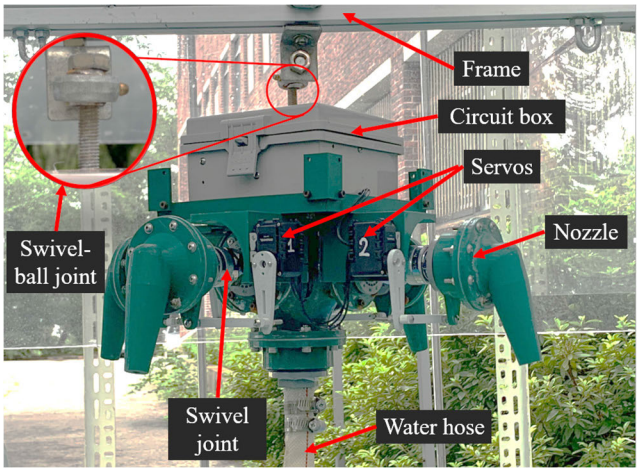

FIGURE 4. The head assembly model hanging on the frame.

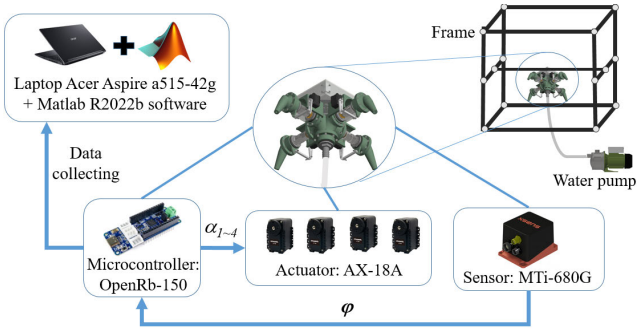

FIGURE 5. The block diagram of the experiment.

TABLE 3. Specification of the system.

Parameter	Description	Value	Unit
$\boldsymbol{J}$	Moment of inertia of the head	$diag\{41956, 41094, 62980\}\times10^{-6}$	kg.m^2
a	Inner cross-sectional area of the outlet nozzle ports	2.8274×10^{-5}	m^2
l , h , d	Dimensions of the head part	153.159×10^{-3}, 78.159×10^{-3}, 98×10^{-3}	m
δ	Folded angle between nozzle and horizontal plane	75	deg
$\dot{m}_0$	Water of mass flow rate	2	kg/s

MTi-680G sensor. The sample time is set to 0.01 [s]. After calculation, the microcontroller sends the control signals to four Dynamixel AX-18A servos. Additionally, Matlab Simulink 2022Rb software is used on an Acer Aspire a515-42g laptop with an AMD Ryzen 5500U processor, 32 [Gb] DDR4 RAM clocked at 3200 [MHz], and an NVIDIA GeForce GTX 1650 graphics card for reading data via a serial communication protocol. The system operates with a baudrate of 921.6 [Kbps]. The experimental diagram is shown in Fig. 5.

TABLE 4. Controller's gains.

ESO's gains	$\boldsymbol{\omega}_0 = diag\{15,15,15\}$
ISTSMC's gains	$\boldsymbol{n}_1 = diag\{35,35,17\}$, $\boldsymbol{n}_2 = diag\{0.1,0.1,0.1\}$, $\boldsymbol{n}_3 = diag\{30,30,25\}$, $\boldsymbol{n}_4 = diag\{45,45,10\}$, $\kappa = 6$

TABLE 5. erformance indexes of step-like reference.

	ISTSMC + ESO	ISTSMC
$RMSE_\phi$ [deg]	0.1180	0.2203
$RMSE_\theta$ [deg]	0.1514	0.1259
$RMSE_\psi$ [deg]	0.7470	1.3225
ISV [deg^2]	2.0969×10^6	3.3064×10^6

B. EXPERIMENTAL RESULTS

In the experiments, the proposed ISTSMC-ESO is compared with the standalone ISTSMC through two scenarios: following the step-like reference and the sinusoidal reference. In both references, the amplitude of the roll and pitch angles are set at ±1.15 [deg], while the yaw angle follows a reference with an amplitude of ±17.2 [deg]. The experiments are conducted over a duration of 45 [s]. The performance of the control system is validated using the root mean square error (RMSE) and integral of the square value (ISV), which are formed below:

$$RMSE_h = \sqrt{\frac{1}{n}\sum_{i=1}^{n} e_h^2} \quad h = \phi, \theta, \psi \tag{29}$$

$$ISV = \sum_{i=1}^{4}\int_0^t \alpha_i^2 dt \quad i = 1, 2, 3, 4 \tag{30}$$

In particular, Fig. 6 to Fig. 10 represent the collected data corresponding to step-like reference, while Fig. 11 to Fig. 15 represent the data for sinusoidal reference, respectively. Specifically, the angular motion control responses of the head assembly are shown in Fig. 6 and Fig. 11. The controlled torques along each roll, pitch, and yaw are shown in Fig. 7 and Fig. 12. The tracking errors are illustrated in Fig. 8 and Fig. 13. The estimated states are presented in Fig. 9 and Fig. 14, and the estimated disturbances are indicated in Fig. 10 and Fig. 15. Moreover, in order to highlight the efficiency of the proposed controller, two performance indexes including RMSE and ISV, are presented in Table 5 and Table 6.

The two controllers provide the system with good tracking performance and robustness against disturbances. In particular, by integrating the rotational dynamics characteristics

TABLE 6. Performance indexes of sinusoidal reference.

	ISTSMC + ESO	ISTSMC
$RMSE_{\phi}$ [deg]	0.1259	0.1419
$RMSE_{\theta}$ [deg]	0.1955	0.1957
$RMSE_{\psi}$ [deg]	1.0121	2.1317
ISV [deg^2]	3.1867×10^6	3.5306×10^6

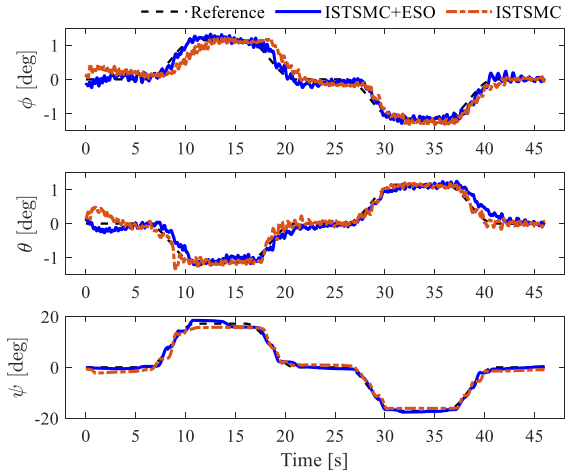

FIGURE 6. Angular motion performance of the head assembly in step-like trajectories.

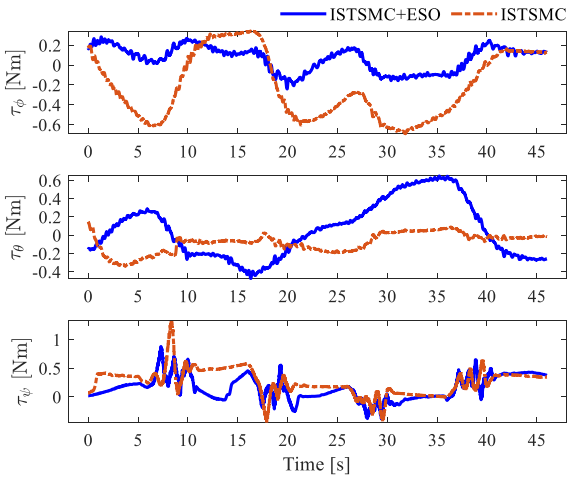

FIGURE 7. Torque distribution along each roll, pitch, and yaw channel in step-like trajectories.

along with the super-twisting algorithm in the control law, one can observe that the controlled output of the two control systems closely follows the desired reference in both scenarios depicted in Fig. 6 and Fig. 11, even in the presence of disturbances. In more detail, during the first half of the tracking process, the roll motion control response of the ISTSMC exhibits a slight lag in the step-like trajectory. This lag is also evident from 5 to 20 [s] in the pitch motion of both controllers in the sinusoidal trajectory. Additionally,

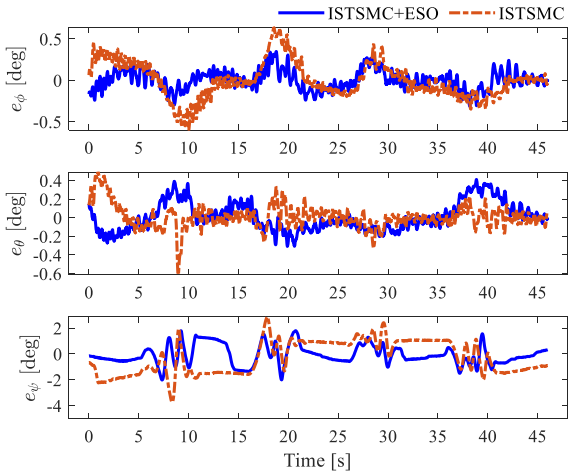

FIGURE 8. Tracking errors in step-like trajectories.

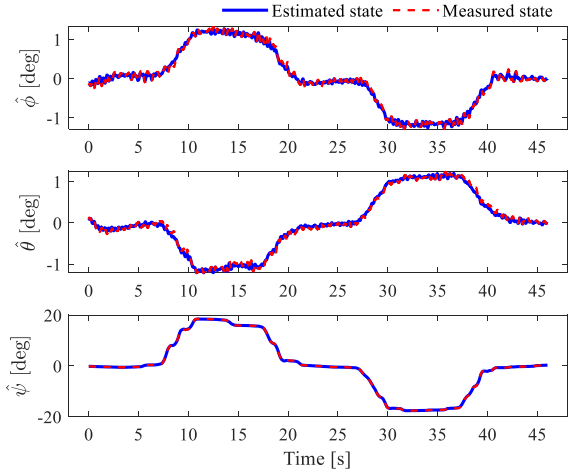

FIGURE 9. State estimation in step-like trajectories.

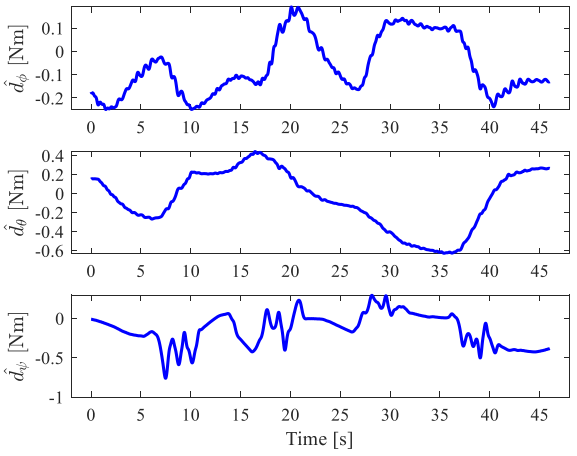

FIGURE 10. Disturbances estimation in step-like trajectories.

during the initial phase from 0 to 7 [s], the yaw motion of the ISTSMC slightly deviates from the origin in both scenarios. This initial deviation is also observed in the roll

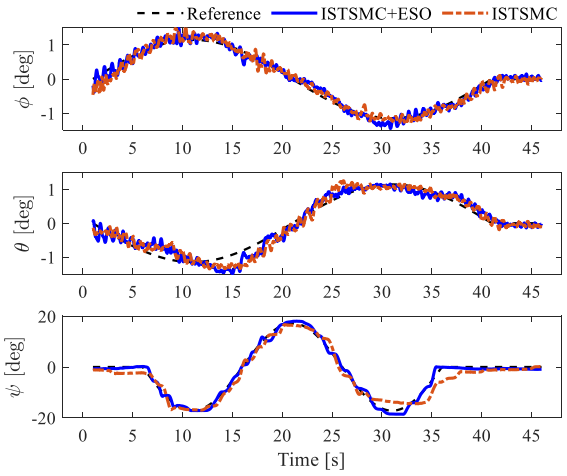

FIGURE 11. Angular motion performance of the head assembly in sinusoidal trajectories.

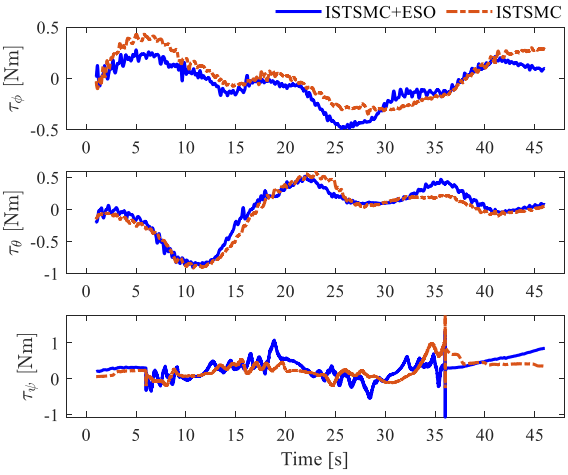

FIGURE 12. Torque distribution along each roll, pitch, and yaw channel in sinusoidal trajectories.

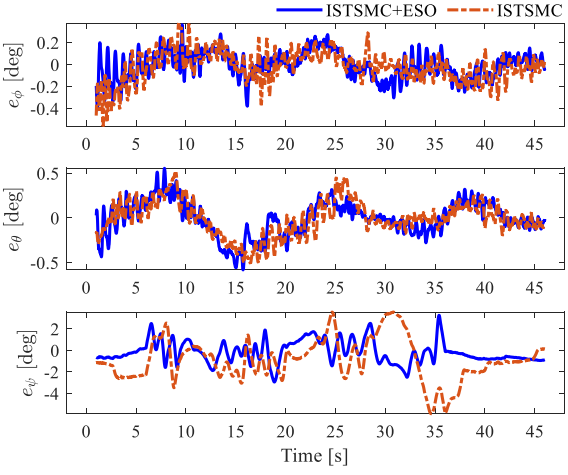

FIGURE 13. Tracking errors in sinusoidal trajectories.

and pitch from 0 to 5 [s] in the step-like trajectory. On the other hand, the yaw motion experiences a bit of overshoot

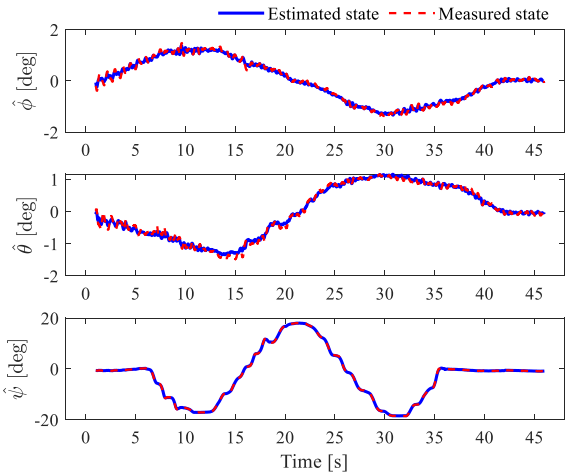

FIGURE 14. State estimation in sinusoidal trajectories.

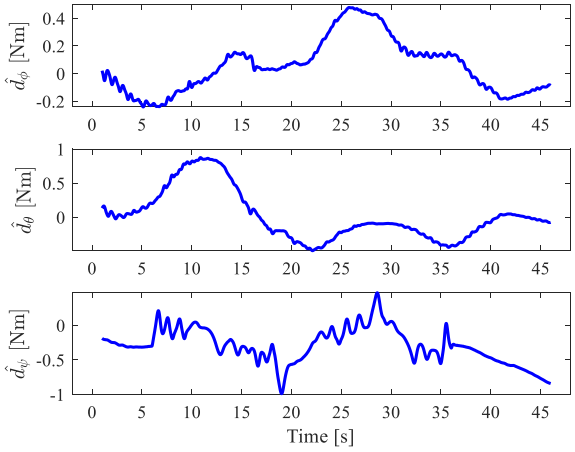

FIGURE 15. Disturbances estimation in sinusoidal trajectories.

from 10 to 15 [s] in the step-like trajectory with the proposed controller. Additionally, the proposed controller requires less overall control effort than the ISTSMC in both scenarios, as illustrated in Fig. 7 and Fig. 12. Furthermore, the proposed controller exhibits lower tracking errors compared to the ISTSMC, as shown in Fig. 8 and Fig. 13. These results indicate the proposed controller provides a better tracking performance with less control effort.

In addition, two performance indexes, namely RMSE and ISV, have been calculated to emphasize the superiority of the proposed controller. A detailed comparison can be found in Tables 5 and 6. Specifically, with the step-like trajectory, compared to the ISTSTMC, the proposed controller exhibits the RMSE_φ and RMSE_ψ values that are approximately less than half, while the RMSE_θ is slightly higher. Overall, the RMSE index of the proposed control system is reduced by up to 56.98% compared to that of the standalone ISTSMC. Moreover, in the case of the sinusoidal trajectory, the RMSE index for each rotation of the proposed control system is significantly lower than that of the standalone ISTSMC, with the yaw motion being twice as low. Additionally, the ISV index

in both scenarios of the ISTSMC is higher than that of the proposed controller, indicating that the proposed controller requires less control effort, with a reduction of up to 22.72%.

Unfortunately, the oscillation of the water hose causes chattering in the controlled output, especially in roll and pitch, as can be seen from Fig. 6 and Fig. 11. Despite being within the bandwidths of the ESO, this fluctuation cannot be attenuated due to the dead-zone of the actuator. Additionally, the influence of the twisted water hose also limits the operating range of yaw motion.

V. CONCLUSION

This paper has proposed a novel unmanned water-powered aerial vehicle using the nozzle rotation mechanism. The purpose of this UWAV is to enhance the utilization of autonomous water-jet propulsion devices in specialized applications, particularly in rescue and firefighting operations. The mathematical model of the head assembly was derived in detail to describe its rotational dynamic characteristics.

Then, a robust nonlinear controller was developed for governing the rotational motions of the head assembly. The ESO plays a role in estimating and compensating for disturbances in the control effort. The ISTSMC ensures system stability and robust tracking. Experiments were conducted to validate the effectiveness of the proposed controller. The experimental results show the superiority of the proposed controller in terms of robustness, tracking performance, and control effort.

At present, the experiments reveal the inevitable influence of the water hose, which causes fluctuations in the head assembly motion. Moreover, the servo arm design of the nozzle rotation mechanism is limited to ± 45 [deg]. In future work, the following improvements will be considered: (1) utilizing the belt drive mechanism to provide an unlimited nozzle rotation range, (2) exploring dead-zone control methods and further attenuating the influence of the water hose, and (3) investigating solutions to eliminate the twisting of the water hose.

ACKNOWLEDGMENT

(Cao-Tri Dinh and Thinh Huynh contributed equally to this work.)

REFERENCES

[1] J. H. Gerken and G. Bright, "Design of a semi-autonomous water-driven flight platform," in *Proc. 24th Int. Conf. Mechatronics Mach. Vis. Pract. (MVIP)*, Auckland, New Zealand, Nov. 2017, pp. 1–6.

[2] F. Jetpack-Zapata, "Maneuvering and stability control system for jetpack," U.S. Patent 0 103 165, Apr. 17, 2014.

[3] R. Li, "Personal propulsion device 2007," U.S. Patent 7 900 867, Mar. 8, 2011.

[4] *Jetlev—Flyer Flight Package*. Accessed: Jul. 20, 2023. [Online]. Available: https://jetlev-flyer.com/

[5] *Jetovator*. Accessed: Jul. 20, 2023. [Online]. Available: https://www.jetovator.com/shop/

[6] *Jet Bike—Zapata*. Accessed: Jul. 20, 2023. [Online]. Available: https://aquaticaviation.net/flyride-the-new-flying-water-jet-bike-from-zapata/

[7] B. Robinson, "Water propelled flying board," U.S. Patent 91 452 06B1, Sep. 29, 2015.

[8] *Jetboard*. Accessed: Jul. 20, 2023. [Online]. Available: https://www.x-jetpacks.com/

[9] *Dubai Firefighters Use Jetpacks to Aid High-Speed Response-Euronews*. Accessed: Jul. 20, 2023. [Online]. Available: https://www.youtube.com/watch?v=H1VIxUTzb1I

[10] C.-T. Dinh, T. Huynh, and Y.-B. Kim, "LQI control system design with GA approach for flying-type firefighting robot using waterpower and weight-shifting mechanism," *Appl. Sci.*, vol. 12, no. 18, p. 9334, Sep. 2022.

[11] X. Liu and H. Zhou, "Unmanned water-powered aerial vehicles: Theory and experiments," *IEEE Access*, vol. 7, pp. 15349–15356, 2019.

[12] D.-H. Lee, T. Huynh, Y.-B. Kim, and C. Soumayya, "Motion control system design for a flying-type firefighting system with water jet actuators," *Actuators*, vol. 10, no. 10, p. 275, Oct. 2021.

[13] T. Huynh and Y.-B. Kim, "Motion control system design for a novel water-powered aerial system for firefighting with flow-regulating actuators," *Drones*, vol. 7, no. 3, p. 162, Feb. 2023.

[14] H. Ando, Y. Ambe, A. Ishii, M. Konyo, K. Tadakuma, S. Maruyama, and S. Tadokoro, "Aerial hose type robot by water jet for fire fighting," *IEEE Robot. Autom. Lett.*, vol. 3, no. 2, pp. 1128–1135, Apr. 2018.

[15] T. Yamaguchi, Y. Ambe, H. Ando, M. Konyo, K. Tadakuma, S. Maruyama, and S. Tadokoro, "A mechanical approach to suppress the oscillation of a long continuum robot flying with water jets," *IEEE Robot. Autom. Lett.*, vol. 4, no. 4, pp. 4346–4353, Oct. 2019.

[16] Y. Yamauchi, Y. Ambe, M. Konyo, K. Tadakuma, and S. Tadokoro, "Passive orientation control of nozzle unit with multiple water jets to expand the net force direction range for aerial hose-type robots," *IEEE Robot. Autom. Lett.*, vol. 6, no. 3, pp. 5634–5641, Jul. 2021.

[17] Y. Yamauchi, Y. Ambe, M. Konyo, K. Tadakuma, and S. Tadokoro, "Realizing large shape deformations of a flying continuum robot with a passive rotating nozzle unit that enlarges jet directions in three-dimensional space," *IEEE Access*, vol. 10, pp. 37646–37657, 2022.

[18] Y. Ambe, Y. Yamauchi, M. Konyo, K. Tadakuma, and S. Tadokoro, "Stabilized controller for jet actuated cantilevered pipe using damping effect of an internal flowing fluid," *IEEE Access*, vol. 10, pp. 5238–5249, 2022.

[19] T. Huynh, D.-H. Lee, and Y.-B. Kim, "Study on actuator performance evaluation of aerial water-powered system for firefighting applications," *Appl. Sci.*, vol. 13, no. 3, p. 1965, Feb. 2023.

[20] W. Khalil and E. Dombre, *Modeling Identification and Control of Robots*. London, U.K.: Kogan Page Science, 2015, ch. 5 & 12, pp. 85–115.

[21] F. M. White, *Fluid Mechanics*, 8th ed. New York, NY, USA: McGraw-Hill, 2016.

[22] Z. Gao, "Scaling and bandwidth-parameterization based controller tuning," in *Proc. Amer. Control Conf.*, 2003, pp. 4989–4996.

[23] H. K. Khalil, *Nonlinear Systems*, 3rd ed., Upper Saddle River, NJ, USA: Prentice-Hall, 2002.

[24] A. F. Filippov, *Differential Equations With Discontinuous Right-Hand Side*. Dordrecht, The Netherlands: Kluwer, 1988.

[25] C. Ren, X. Li, X. Yang, and S. Ma, "Extended state observer-based sliding mode control of an omnidirectional mobile robot with friction compensation," *IEEE Trans. Ind. Electron.*, vol. 66, no. 12, pp. 9480–9489, Dec. 2019.

[26] S. Boyd, L. El Ghaoui, E. Feron, and V. Balakrishnan, *Linear Matrix Inequalities in System and Control Theory*. Philadelphia, PA, USA: Society for Industrial and Applied Mathematics, 1994.

[27] L.-W. Chang, "Dynamics of a sliding control with a first-order plus integral sliding condition," *Dyn. Control*, vol. 2, no. 2, pp. 201–219, Apr. 1992.

[28] I.-C. Baik, K.-H. Kim, and M.-J. Youn, "Robust nonlinear speed control of PM synchronous motor using boundary layer integral sliding mode control technique," *IEEE Trans. Control Syst. Technol.*, vol. 8, no. 1, pp. 47–54, Jan. 2000.

[29] S. Seshagiri and H. K. Khalil, "On introducing integral action in sliding mode control," in *Proc. 41st IEEE Conf. Decis. Control*, Dec. 2002, pp. 1473 1478.

[30] H. Jin and X. Zhao, "Approach angle-based saturation function of modified complementary sliding mode control for PMLSM," *IEEE Access*, vol. 7, pp. 126014–126024, 2019.

[31] L. Peng, M. Jian-jun, L. Wen-qiang, and Z. Zhi-qiang, "Adaptive conditional integral sliding mode control for fault tolerant flight control system," in *Proc. 7th Int. Conf. Syst. Simul. Sci. Comput.*, Oct. 2008, pp. 638–642.

[32] L. Fridman, J. Moreno, and R. Iriarte, *Sliding Modes After the First Decade of the 21st Century* (Lecture Notes in Control and Information Sciences), vol. 412. Berlin, Germany: Springer, 2012.
[33] T. Gonzalez, J. A. Moreno, and L. Fridman, "Variable gain super-twisting sliding mode control," *IEEE Trans. Autom. Control*, vol. 57, no. 8, pp. 2100–2105, Aug. 2012.

CAO-TRI DINH was born in Vĩnh Long, Vietnam. He received the engineering degree, in 2019, and the M.Eng. degree in vehicle engineering from the Ho Chi Minh City University of Technology and Education (HCMUTE), Vietnam, in 2021. He is currently pursuing the Ph.D. degree with the Department of Intelligent Robot Engineering, Pukyong National University, Busan, South Korea. Since 2022, he has been a Lecturer with the Department of Automotive Electronics, HCMUTE. His research interests include control systems, autonomous vehicle control engineering, and mobile robot.

THINH HUYNH received the Engineering and M.Eng. degrees in vehicle engineering from the Ho Chi Minh City University of Technology and Education (HCMUTE), Vietnam, in 2014 and 2016, respectively, and the Ph.D. degree from the Department of Smart Robot Convergence and Application Engineering, Pukyong National University (PKNU), Busan, South Korea, in 2022. Since 2017, he has been with the Department of Chassis and Body, HCMUTE, Vietnam. He is currently a Postdoctoral Researcher with the Department of Mechanical System Engineering, PKNU. His research interests include control engineering, robotics, and automotive engineering.

DONG-HUN LEE received the B.S., M.S., and Ph.D. degrees in mechanical system engineering from Pukyong National University (PKNU), Busan, South Korea, in 2017, 2019, and 2021, respectively. He is currently an Assistant Professor with the Department of Mechanical System Engineering, PKNU. His research interests include control theory and application with control system design of marine systems.

YOUNG-BOK KIM (Senior Member, IEEE) received the B.S. and M.S. degrees in mechanical system engineering from Pukyong National University, Busan, South Korea, and the Ph.D. degree from Kobe University, Kobe, Japan, in 1996. He has held a visiting position with the Department of Mechanical Engineering, University of Maryland, Maryland, from 2011 to 2012. He is currently a Professor with the Department of Mechanical System Engineering, Pukyong National University. His research interests include control theory and application with dynamic ship positioning and autonomous control system design. He is a member of ICASE, KSME, and ASME.